

# Detection of Marine Borne Radioactive Sources Report

September 2022

Johns, Jesse M (PI)  
Archambault, Brian C  
Bernacki, Bruce E  
Gorecke, Kevin C  
Hossbach, Todd W  
Hughes, Michael S  
Krogstad, Eirik J  
Loer, Ben M  
Maxwell, Adam R  
Quint, Marc C  
Spadoni, Franco L

## DISCLAIMER

This report was prepared as an account of work sponsored by an agency of the United States Government. Neither the United States Government nor any agency thereof, nor Battelle Memorial Institute, nor any of their employees, **makes any warranty, express or implied, or assumes any legal liability or responsibility for the accuracy, completeness, or usefulness of any information, apparatus, product, or process disclosed, or represents that its use would not infringe privately owned rights.** Reference herein to any specific commercial product, process, or service by trade name, trademark, manufacturer, or otherwise does not necessarily constitute or imply its endorsement, recommendation, or favoring by the United States Government or any agency thereof, or Battelle Memorial Institute. The views and opinions of authors expressed herein do not necessarily state or reflect those of the United States Government or any agency thereof.

PACIFIC NORTHWEST NATIONAL LABORATORY  
*operated by*  
BATTELLE  
*for the*  
UNITED STATES DEPARTMENT OF ENERGY  
*under Contract DE-AC05-76RL01830*

Printed in the United States of America

Available to DOE and DOE contractors from  
the Office of Scientific and Technical  
Information,  
P.O. Box 62, Oak Ridge, TN 37831-0062  
[www.osti.gov](http://www.osti.gov)  
ph: (865) 576-8401  
fox: (865) 576-5728  
email: [reports@osti.gov](mailto:reports@osti.gov)

Available to the public from the National Technical Information Service  
5301 Shawnee Rd., Alexandria, VA 22312  
ph: (800) 553-NTIS (6847)  
or (703) 605-6000  
email: [info@ntis.gov](mailto:info@ntis.gov)  
Online ordering: <http://www.ntis.gov>

# Detection of Marine Borne Radioactive Sources Report

[Click here to enter text.](#)

September 2022

Johns, Jesse M (PI)  
Archambault, Brian C  
Bernacki, Bruce E  
Gorecke, Kevin C  
Hossbach, Todd W  
Hughes, Michael S  
Krogstad, Eirik J  
Loer, Ben M  
Maxwell, Adam R  
Quint, Marc C  
Spadoni, Franco L

Prepared for  
the U.S. Department of Energy  
under Contract DE-AC05-76RL01830

Pacific Northwest National Laboratory  
Richland, Washington 99354

## Abstract

This report describes a preliminary analysis on the utility of modern capabilities to localize radiological sources in a marine environment. This study analyzed expected background sources and identified possible approaches based on modeling and simulation analyses. The effort culminated in the design and fabrication of validation experiments which provided favorable supporting data. The conclusions of this effort are not conclusive as to the viability of the approach, but neither is the underlining hypothesis disproved. Continuation of the experimental approach is recommended with a focus on open-water experimentation.

## Acknowledgments

This research was supported by the Open Call Initiative under the Laboratory Directed Research and Development (LDRD) Program at Pacific Northwest National Laboratory (PNNL). PNNL is a multi-program national laboratory operated for the U.S. Department of Energy (DOE) by Battelle Memorial Institute under Contract No. DE-AC05-76RL01830.

## Contents

Abstract .....	1
Acknowledgments.....	2
Contents.....	3
1.0 Introduction.....	5
1.1 Cherenkov Radiation .....	5
1.2 Background Light Sources.....	5
2.0 Modeling and Evaluation .....	6
2.1 Point source .....	6
2.1.1 Volumetric source.....	7
2.1.2 Sea Water Model.....	8
3.0 Experimental Setup.....	11
4.0 Conclusions.....	14

## Figures

Figure 1. Index of refraction, electron stopping power, and absorption constant of seawater .....	8
Figure 2. Total Cherenkov photons produced in seawater for an incident electron of a given energy, and normalized spectral emission for electrons of 0.4 and 3 MeV .....	9
Figure 3: Normalized spectrum from Cherenkov emission of a 3 MeV electron as a function of distance from a point source .....	9
Figure 4. $^{40}\text{K}$ beta decay spectrum and resulting Cherenkov photon spectrum, comparing reference and calculation to results from GEANT4.....	10
Figure 5. Left: Total photon flux from $^{30}\text{K}$ decays in seawater as a function of the total distance considered, assuming 12 Bq/L (400ppm * 31 mBq/kg/ppm). Right: Integrated spectrum of the total visible volume of K40 Cherenkov emissions. ....	10
Figure 6. 3D rendering of the experimental setup, showing the water tube, inlet/outlets, and mixing tank.....	11
Figure 7. Laboratory experimental setup. Shown is a representative source with the water tube covered with "light-tight" cloth. ....	12
Figure 8. Experiment data results over a series of weeks for a source near (6 inches) and far (30 inches) from the photon-multiplier tube (PMT) detector. ....	12
Figure 9. Geant4 modeling comparison of background photons from Muons and natural radiological decay compared to experimental results. ....	13

## 1.0 Introduction

The UMBRA project is evaluating the practical limitations of utilizing radiation-induced Cherenkov photon detection to enable radiological source discovery in the deep ocean. This approach can provide an unprecedented capability to detect radiological materials in the ocean. The purpose of this effort is to define the theoretical and practical limitations inherent with this capability, while also generating models and experimental data to identify and evaluate methods for detection and localization of sources of interest. This report evaluates the potential for Cherenkov photon detection to detect, discrete, and locate sources by utilizing sensitive photon detection sensors and systematically addressing background subtraction techniques.

### 1.1 Cherenkov Radiation

The Cherenkov emission rate and spectrum are given by <sup>1</sup>:

$$\frac{d^2N}{d\lambda dE} = 2\pi\alpha \left(1 - \frac{1}{\beta^2 n^2(\lambda)}\right) \frac{1}{\lambda^2}$$

Where  $\alpha$  is the fine structure constant,  $\beta$  is the particle's velocity divided by the speed of light, and  $n$  is the index of refraction as a function of wavelength  $\lambda$ . Energy loss from Cherenkov production is negligible compared to ionization and multiple scattering. The total number of photons emitted for an incident particle of energy  $E_0$  is

$$N(E_0) = 2\pi\alpha \int_{E_t}^{E_0} \int_{n\beta > 1} \left(1 - \frac{1}{\beta^2 n^2}\right) \frac{1}{\lambda^2} \left(\frac{dE}{dx}\right)^{-1} d\lambda dE$$

Where  $E = mc^2(\gamma - 1)$  is the kinetic energy,  $\gamma = \sqrt{1/(1 - \beta^2)}$ , and  $E_t$  is the threshold kinetic energy corresponding to  $\beta_t = 1/n$ .  $dE/dx$  is the stopping power and is a function of energy.

### 1.2 Background Light Sources

Cherenkov light is not inherently unique, and it is therefore necessary to determine and model the appropriate background light sources that would impede detection of the generating radiological source. This section describes the expected background sources that were modeled for this effort.

The primary sources of background light considered in this effort include:

- Ocean salinity/Potassium-40 (Appendix A.1.1)
- Cosmic muons
- Bioluminescence (Appendix A.1.2)
- Solar illumination

---

<sup>1</sup> E. Ciarrocchi and N. Belcari, *Cherenkov Luminescence Imaging: Physics Principles and Potential Applications in Biomedical Sciences*, EJNMMI Physics **4**, 14 (2017).

## 2.0 Modeling and Evaluation

In this section, we estimate the rate of observable photon fluxes produced by Cherenkov emission from energetic particles in seawater, as a function of distance from the source. Here we assume that the background is dominated by beta decay of  $^{40}\text{K}$  distributed uniformly throughout the seawater, and the primary source of interest are thermal neutrons capturing on elements in the water. Other likely sources of background and mitigation strategies are discussed in other sections, but this simplifying assumption is utilized for initial model development.

We approach this estimation in two ways: a calculation from first principles (incorporating standard reference datasets where analytical formulas are not appropriate), and using GEANT4<sup>1</sup>, a Monte Carlo simulation-based radiation transport library.

### 2.1 Point source

A photosensor of area  $\sigma$  is placed a distance  $D$  from a light-emitting source. The source emits  $R_0$  photons per second isotropically with a spectrum  $dN/d\lambda$ . The intervening medium attenuates the light with spectral attenuation coefficients  $A(\lambda)$ . The photodetector has spectral quantum efficiency  $Q(\lambda)$ . The count rate of the photodetector is

$$R = \frac{R_0 \sigma}{4\pi D^2} \int \frac{dN}{d\lambda} Q(\lambda) e^{-A(\lambda)D} d\lambda$$

For given emission, absorption, and quantum efficiency spectra, the integral term can be pre-computed:

$$\bar{A}(D) = \int \frac{dN}{d\lambda} Q(\lambda) e^{-A(\lambda)D} d\lambda$$

$$R = \frac{R_0 \sigma \bar{A}(D)}{4\pi D^2}$$

At long distances,  $\bar{A}$  will be dominated by the minimum attenuation wavelength. If the source is at an angle to the photodetector with a flat face, there is a reduction in the effective solid angle

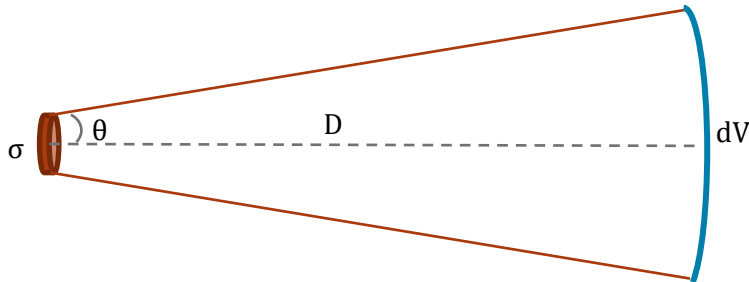
---

<sup>1</sup> S. Agostinelli, J. Allison, K. Amako, J. Apostolakis, H. Araujo, P. Arce, M. Asai, D. Axen, S. Banerjee, G. Barrand, F. Behner, L. Bellagamba, J. Boudreau, L. Broglia, A. Brunengo, H. Burkhardt, S. Chauvie, J. Chuma, R. Chytracsek, G. Cooperman, G. Cosmo, P. Degtyarenko, A. Dell'Acqua, G. Depaola, D. Dietrich, R. Enami, A. Feliciello, C. Ferguson, H. Fesefeldt, G. Folger, F. Foppiano, A. Forti, S. Garelli, S. Giani, R. Giannitrapani, D. Gibin, J. J. Gómez Cadenas, I. González, G. Gracia Abril, G. Greeniaus, W. Greiner, V. Grichine, A. Grossheim, S. Guatelli, P. Gumplinger, R. Hamatsu, K. Hashimoto, H. Hasui, A. Heikkinen, A. Howard, V. Ivanchenko, A. Johnson, F. W. Jones, J. Kallenbach, N. Kanaya, M. Kawabata, Y. Kawabata, M. Kawaguti, S. Kelner, P. Kent, A. Kimura, T. Kodama, R. Kokoulin, M. Kossov, H. Kurashige, E. Lamanna, T. Lampén, V. Lara, V. Lefebure, F. Lei, M. Liendl, W. Lockman, F. Longo, S. Magni, M. Maire, E. Medernach, K. Minamimoto, P. Mora de Freitas, Y. Morita, K. Murakami, M. Nagamatu, R. Nartallo, P. Nieminen, T. Nishimura, K. Ohtsubo, M. Okamura, S. O'Neale, Y. Oohata, K. Paech, J. Perl, A. Pfeiffer, M. G. Pia, F. Ranjard, A. Rybin, S. Sadilov, E. Di Salvo, G. Santin, T. Sasaki, N. Savvas, Y. Sawada, S. Scherer, S. Sei, V. Sirotenko, D. Smith, N. Starkov, H. Stoecker, J. Sulikimo, M. Takahata, S. Tanaka, E. Tcherniaev, E. Safai Tehrani, M. Tropeano, P. Truscott, H. Uno, L. Urban, P. Urban, M. Verderi, A. Walkden, W. Wander, H. Weber, J. P. Wellisch, T. Wenaus, D. C. Williams, D. Wright, T. Yamada, H. Yoshida, and D. Zschesche, *Geant4—a Simulation Toolkit*, Nuclear Instruments and Methods in Physics Research Section A: Accelerators, Spectrometers, Detectors and Associated Equipment **506**, 250 (2003).

$$\sigma_{eff} = \sigma \cos \phi$$

## 2.2 Volumetric source

The medium surrounding the photodetector is both light emitting and attenuating. We will ignore scattering for now. The photodetector has a viewing half-angle  $\theta$ . The average light production is  $R_V$  photons per second per unit volume. The volume of the infinitesimal element a distance  $D$  from the sensor, where  $D$  is large compared to the photodetector size, is



$$dV = 2\pi D^2(1 - \cos \theta)dD$$

For a flat photodetector face, the integrated effective area is

$$\sigma_{eff} = \frac{\sigma(1 + \cos \theta)}{2}$$

The average count rate for the volume element  $dV$  is

$$dR = \frac{R_0 \sigma_{eff} \bar{A}(D)}{4\pi D^2} dV$$

And the total count rate seen by the sensor is

$$R = \frac{R_0 \sigma \sin^2 \theta}{4} \int_0^\infty \bar{A}(D) dD$$

For a flat face and

$$R = \frac{R_0 \sigma (1 - \cos \theta)}{2} \int_0^\infty \bar{A}(D) dD$$

For a spherical face, where  $R_0$  is in photons per unit time per volume.

## 2.3 Sea Water Model

Figure 1 shows the index of refraction and total electron stopping power for seawater, calculated assuming a density of  $1.025 \text{ g/cm}^3$  and a material composition of 85.6% O, 10.8% H, 1.99% Cl, 1.1% Na, 0.1% Mg, 0.09% S, and 0.04% K<sup>12</sup>.

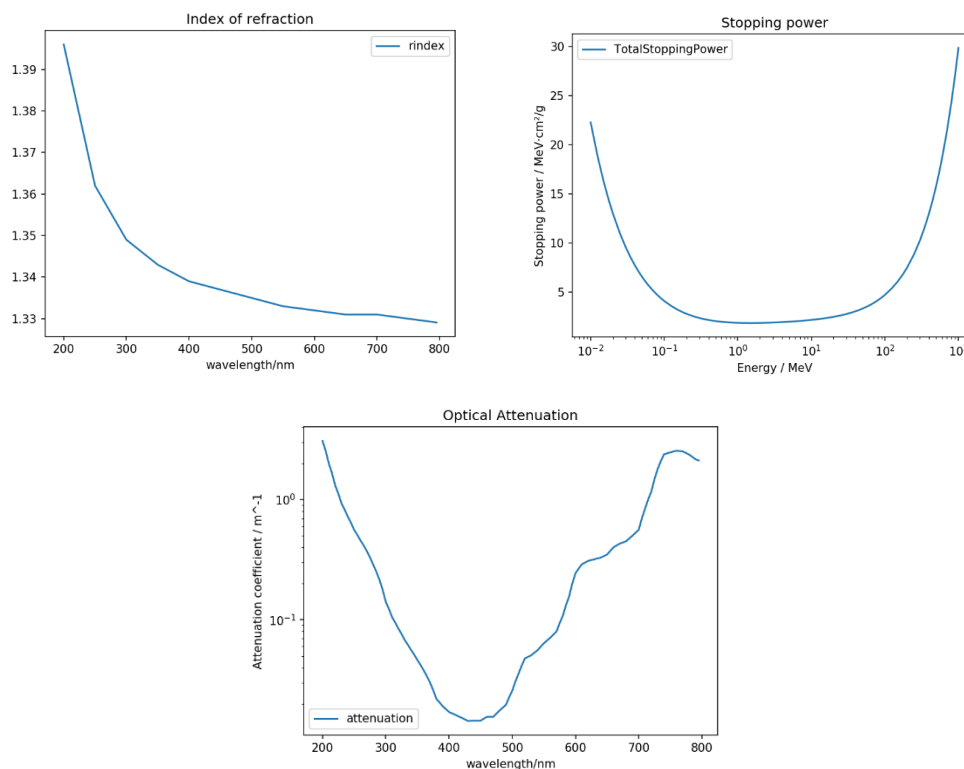


Figure 1. Index of refraction, electron stopping power, and absorption constant of seawater<sup>34</sup>.

Figure 2 shows the total number and spectral distribution of Cherenkov photons produced by an electron in seawater.

<sup>1</sup> J. E. Huheey, E. A. Keiter, and R. L. Keiter, *Inorganic Chemistry: Principles of Structure and Reactivity*, 4. ed., [repr.] (Harper, Cambridge, 2009).

<sup>2</sup> R. C. Weast, editor, *Handbook of Chemistry and Physics: A Ready-Reference Book of Chemical and Physical Data*, 55. ed., 1974–1975 (CRC Press, Cleveland, Ohio, 1974).

<sup>3</sup> M. J. Berger, J. S. Coursey, M. A. Zucker, and J. Chang, *ESTAR, PSTAR, and ASTAR: Computer Programs for Calculating Stopping-Power and Range Tables for Electrons, Protons, and Helium Ions* (2005).

<sup>4</sup> R. C. Smith and K. S. Baker, *Optical Properties of the Clearest Natural Waters (200–800 Nm)*, *Appl. Opt.*, AO **20**, 177 (1981).

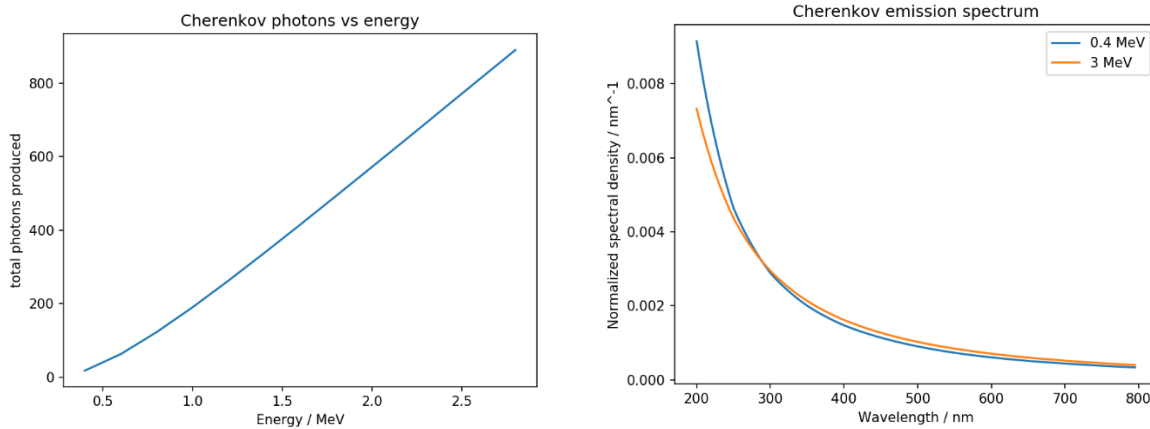


Figure 2. Total Cherenkov photons produced in seawater for an incident electron of a given energy, and normalized spectral emission for electrons of 0.4 and 3 MeV

Figure 3 shows the Cherenkov photon energy spectrum shift with distance from a source.

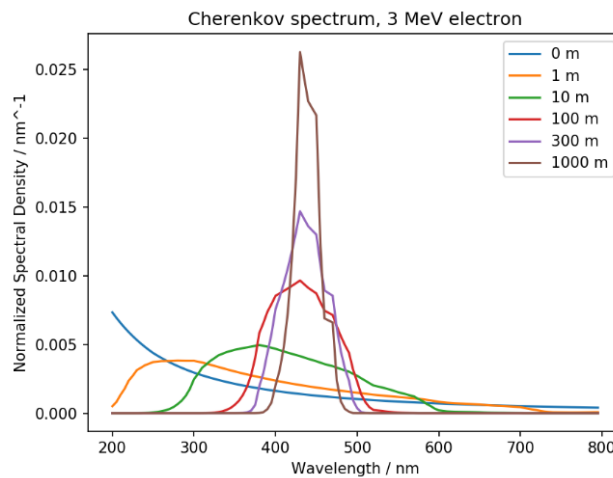


Figure 3: Normalized spectrum from Cherenkov emission of a 3 MeV electron as a function of distance from a point source

Figure 4 compares a reference <sup>40</sup>K beta decay spectrum<sup>1</sup> and the calculated Cherenkov emission rate and spectrum to the values produced by the GEANT4 simulation. Note that, although GEANT4 produces a noticeably different beta decay spectrum, the Cherenkov emission is almost identical. The calculated Cherenkov total photon emission is 74.9 photons per decay (considering only the 89.3% beta-decay branching ratio), compared to 76.9 produced by GEANT4 simulation.

<sup>1</sup> W. H. Kelly, G. B. Beard, and R. A. Peters, *The Beta Decay of K40*, Nuclear Physics **11**, 492 (1959).

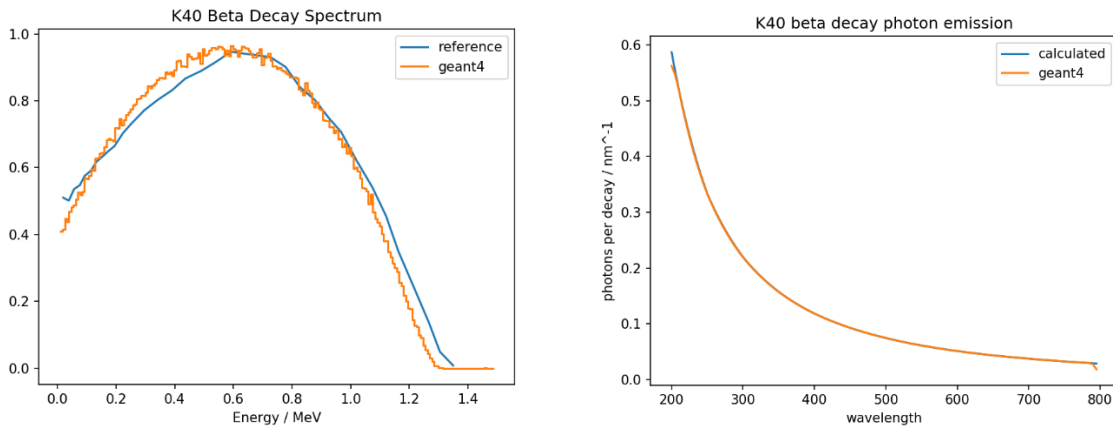


Figure 4. <sup>40</sup>K beta decay spectrum and resulting Cherenkov photon spectrum, comparing reference<sup>1</sup> and calculation to results from GEANT4

Figure 5 shows the total photon flux through a flat surface with 90 degree acceptance half-angle for 12 Bq/L of <sup>40</sup>K decay, as a function of the total distance considered. The dashed red line is the result from a GEANT4 simulation of <sup>40</sup>K decays uniformly placed throughout a 3 km radius sphere of seawater bisected by a flat plane photodetector. The small discrepancy could be due to Rayleigh scattering, which is modeled in GEANT4 but not considered in these calculations, or differences in interpolating datasets.

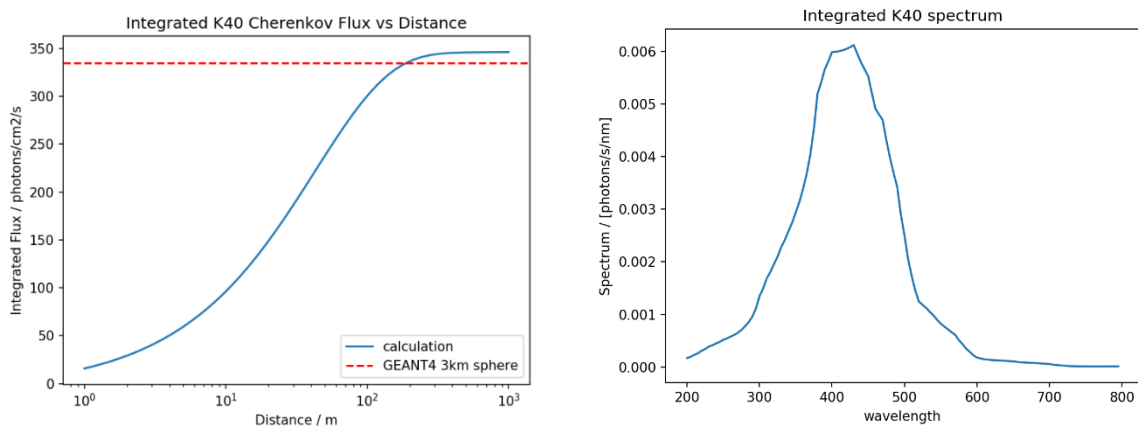


Figure 5. Left: Total photon flux from <sup>30</sup>K decays in seawater as a function of the total distance considered, assuming 12 Bq/L (400ppm \* 31 mBq/kg/ppm). Right: Integrated spectrum of the total visible volume of K40 Cherenkov emissions.

<sup>1</sup> W. H. Kelly, G. B. Beard, and R. A. Peters, *The Beta Decay of K40*, Nuclear Physics **11**, 492 (1959).

### 3.0 Experimental Setup and Validation

The validation experimental setup is simply a water-containing tube with open ends for detector mounting (Figure 6). The tube includes fill and discharge lines to enable straight-forward exchange and mixing of solution-carrying water. This allows for changes of salinity without requiring significant changes to the setup. The tube is lined internally with Teflon to improve reflectivity, and it is lined externally with “light-tight” cloth to reduce light contamination from office lighting (Figure 7).

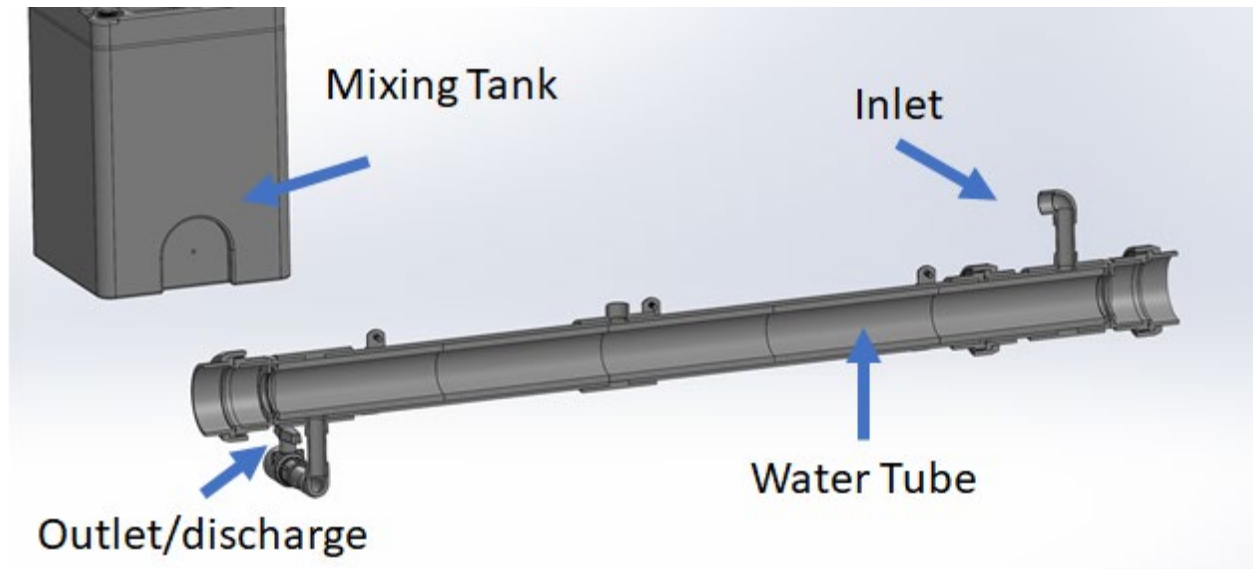


Figure 6. 3D rendering of the experimental setup, showing the water tube, inlet/outlets, and mixing tank.

#### 3.1 Experimental Results

Figure 8 shows a compilation of data from experiments over a series of weeks for a source near (6 inches) and far (30 inches) from the photon-multiplier tube (PMT) detector. Figure 9 shows the comparison of Geant4 background modeling with the experimental system.

Water Tube (with "light-tight" cloth)

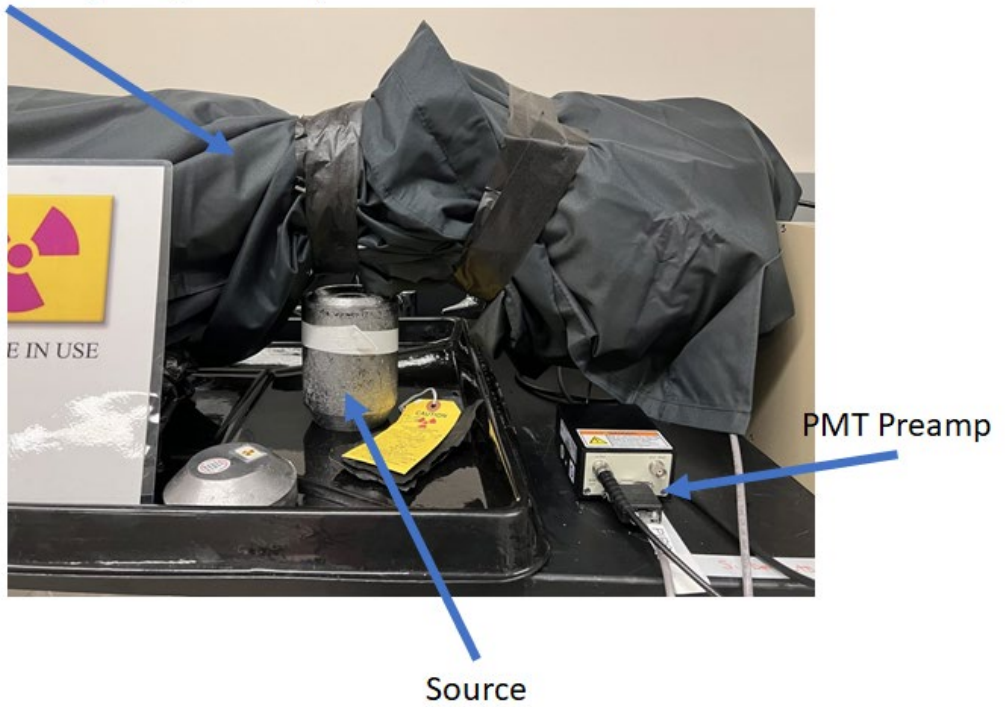


Figure 7. Laboratory experimental setup. Shown is a representative source with the water tube covered with "light-tight" cloth.

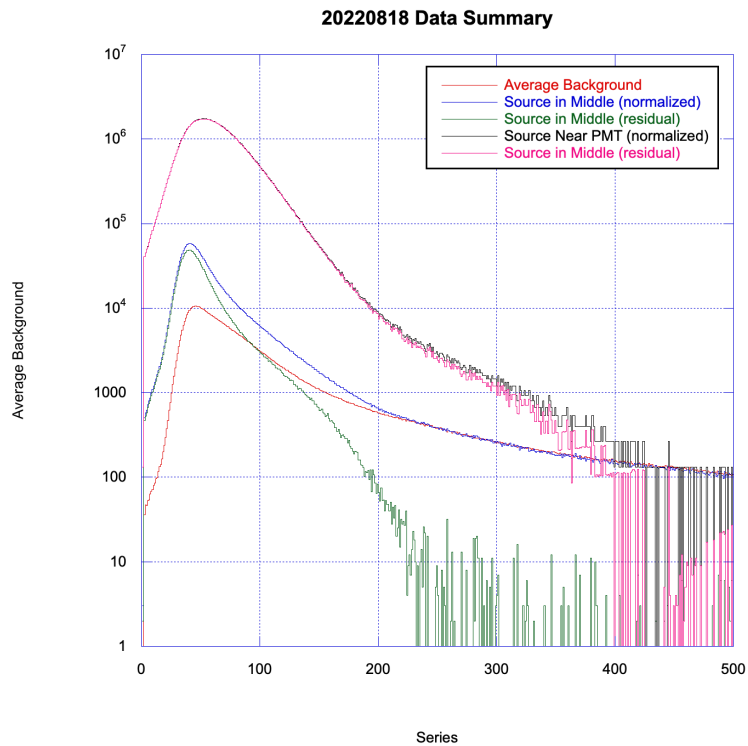


Figure 8. Experiment data results over a series of weeks for a source near (6 inches) and far (30 inches) from the photon-multiplier tube (PMT) detector.

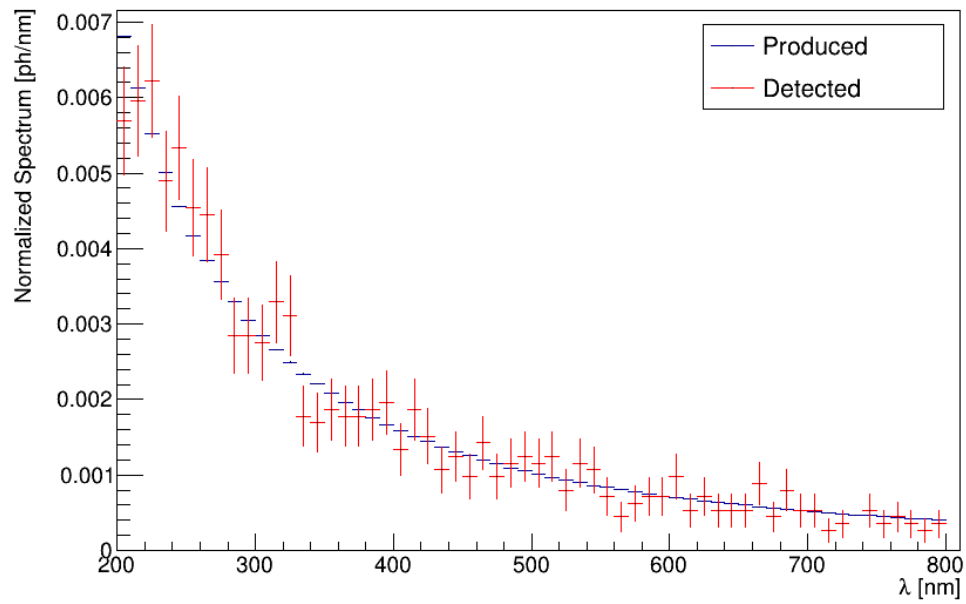


Figure 9. Geant4 modeling comparison of background photons from Muons and natural radiological decay compared to experimental results.

## 4.0 Conclusions

This effort describes a preliminary analysis on the utility of modern capabilities to localize radiological sources in a marine environment. This study analyzed expected background sources and identified possible approaches based on modeling and simulation analyses. The effort culminated in the design and fabrication of validation experiments which provided favorable supporting data. The conclusions of this effort are not conclusive as to the viability of the approach, but neither is the underlining hypothesis disproved. Continuation of the experimental approach is recommended with a focus on open-water experimentation.

An extensive literature review and preliminary system designs were also conducted during this effort. The results of these are provided in the Appendix, to include:

- Ocean Salinity (A.1.1)
- Bioluminescence (A.1.2)
- Effect of Thermoclines on Light Propagation (A.2)
- Effectiveness of Polarization Filtering (A.3)

In addressing polarization and bioluminescence, it is worth noting that there is a significant lack of research in these areas as they related to Cherenkov light. Potential research directions outside of this effort may include these areas, specifically noting that neither phenomenon is well measured/documented in the literature.

## A.1 Background Sources

### A.1.1 Ocean Salinity/Potassium-40

In general, the salinity is highest at the surface, and therefore the background contribution from K-40 is conservative by using surface values.<sup>1</sup> Figure A.1 shows the salinity distribution with the highest concentration in the Mediterranean Sea.

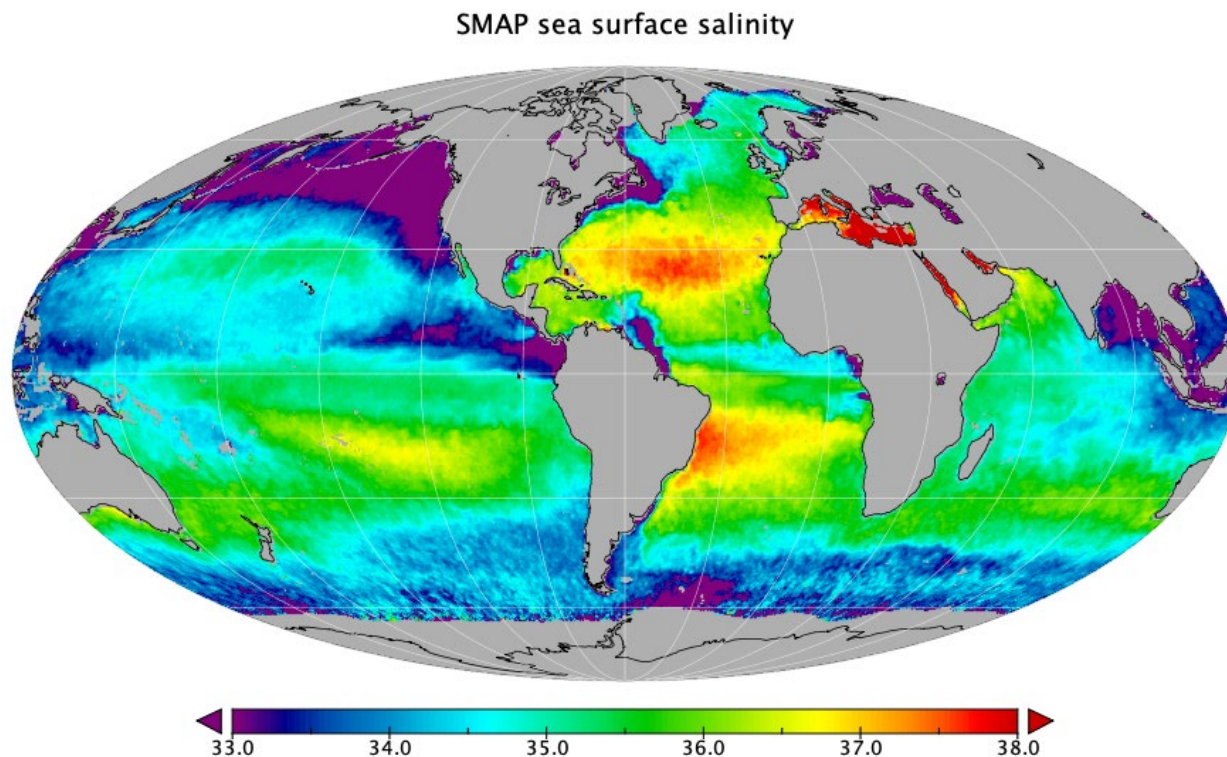


Figure A.1: Surface salinity map of the ocean in October 2021 generated by NASA's Soil Moisture Active Passive mission.<sup>2</sup>

The concentration of major constituents in surface seawater at 35% and 40% salinity are provided in Table A.1.

Table A.1. Concentration of ions in the ocean.<sup>3</sup>

Ion	Concentration at	
	35% S	40% S

<sup>1</sup> L. Talley, *Salinity Patterns in the Ocean*. Encyclopedia of Global Environmental Change. ISBN 0.471.97796-9. Vol 1 pp 629-640. 2002.

<sup>2</sup> <https://salinity.oceansciences.org/smap-salinity.htm>

<sup>3</sup> Pilson, Michael. *An Introduction to the Chemistry of the Sea*. 2<sup>nd</sup> Edition. 1988.

	<b>g/kg</b>	<b>g/kg</b>
Na+	10.781	12.321
K+	0.0399	0.046
Mg <sup>++</sup>	1.284	1.467
Ca <sup>++</sup>	0.4119	0.4707
Sr <sup>++</sup>	0.00794	0.00907
Cl <sup>-</sup>	19.353	22.118
SO <sub>4</sub> <sup>--</sup>	2.712	3.099
HCO <sub>3</sub> <sup>-</sup>	0.126	0.144
Br <sup>-</sup>	0.0673	0.0769
B(OH) <sub>3</sub>	0.0257	0.0294
F <sup>-</sup>	0.0013	0.0015

It is reasonable to assume that the ratio of Na and K is uniform throughout the ocean. Sodium, as the ion Na<sup>+</sup>, is the second most abundant element dissolved in seawater. It is a conservative element, which means that processes that affect sodium concentration in seawater are limited to dilution by rainfall or riverine input, alteration of seafloor, and evaporation.<sup>12</sup> Any losses of Na from these processes are balanced by input from the world's rivers, leading to long-term constancy in ocean Na concentrations. Na concentrations vary only due to differences in evaporation or precipitation. Concentrations are higher in the Atlantic Ocean. The oceanographic half-life of Na is very long, 55 million years. This means that the average time that it takes an atom of Na to be exchanged with other Earth reservoirs is very long with respect to ocean circulation times.

Potassium is the sixth most abundant element dissolved in seawater and, like Na, has a very long residence time, 12 million years. Potassium is present in seawater as the K<sup>+</sup> ion. Like Na, it has a conservative distribution, which means that its concentration varies only due to differences in evaporation or precipitation in the water. Its concentrations vary in waters that sank to form intermediate or deep waters in the sea. As its behavior is very similar to Na, measured Na/K ratios are very constant, reflecting their similar conservative nature. Both elements are added to the oceans by river water. Both are removed in hot, dry climates (e.g., the Persian Gulf) by evaporation.

An analysis of the worst-case background activity from the contribution of naturally occurring <sup>40</sup>K in seawater was performed utilizing the Center for Environmental Data Analysis database, which provides measurements for sea surface salinity from January, 2010 through December 2019.<sup>3</sup>

This gave salinity measurements in practical salinity units (PSU, equal to 1g salt/kg) ranging from 1.71 to 40.00 with a mean value of 34.83 (full distribution shown in Figure A.2). The peak salinity value occurred near 25.0N, 36.2E—in the northern third of the Red Sea.

<sup>1</sup> Culkin, F., and Cox, R. A., 1966. Sodium, potassium, magnesium, calcium and strontium in sea water. *Deep-Sea Res.*, 13: 789-804.

<sup>2</sup> Broecker, W. S. and Peng, T.-H., 1982. Eldigo Press, Palisades, NY

<sup>3</sup> J. Boutin *et al.* *ESA Sea Surface Salinity Climate Change Initiative (Sea\_Surface\_Salinity\_cci): weekly and monthly sea surface salinity products, v2.31, for 2010 to 2019*, doi: [10.5285/4ce685bff631459fb2a30faa699f3fc5](https://doi.org/10.5285/4ce685bff631459fb2a30faa699f3fc5)

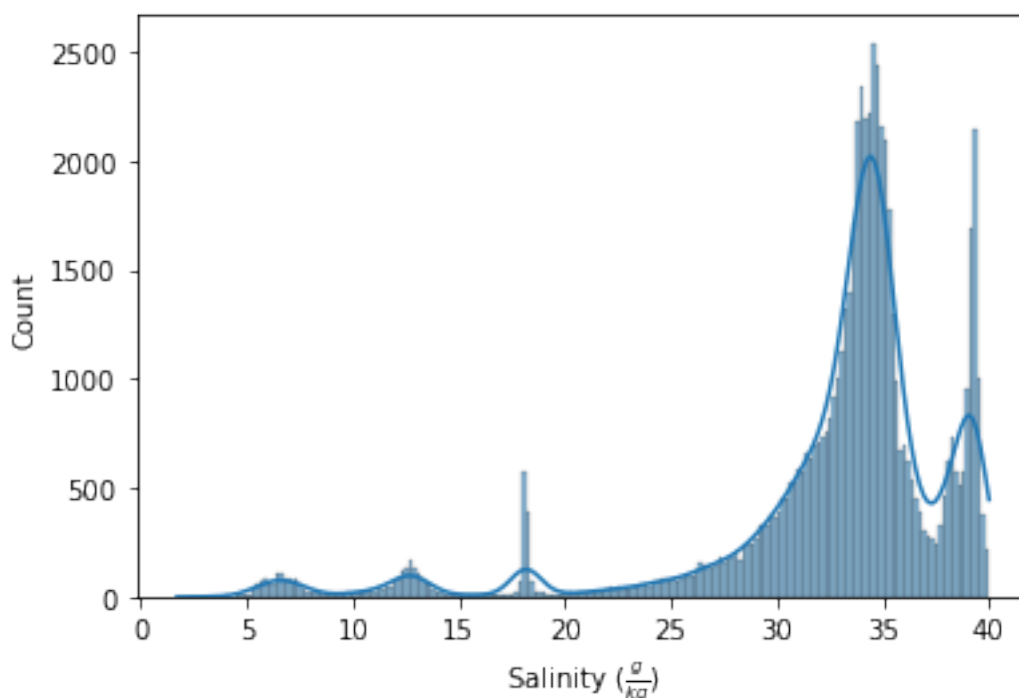


Figure A.2: Distribution of global sea surface salinity measurements. The distribution is strongly peaked around the mean value of 34.8 g/kg. The small peak near 18 g/kg likely corresponds to freshwater inlets (e.g., rivers)

The fraction of this total salinity corresponding to potassium relative to the chlorine concentration is reported as having “no significant regional differences”, with an average and standard deviation of  $0.02023 \pm 0.000032$ .<sup>1</sup> This is consistent with other measurements based on samples at extreme salinity values (in bodies of water corresponding to high measurements).<sup>23</sup> These data sources were combined to predict a conservative upper bound for <sup>40</sup>K concentration in seawater. The conservative concentration of potassium was calculated to be 479ppm. The isotopic composition of potassium is geographically consistent, with a <sup>40</sup>K number fraction of  $1.17 \times 10^{-4}$ , corresponding to a mass fraction of  $1.20 \times 10^{-4}$ , or 57.4ppb <sup>40</sup>K.<sup>4</sup>

### A.1.2 Bioluminescence

Bioluminescence (BL) refers to the generation of light by water-borne organisms that use this capability for purposes ranging from defense to reproduction. BL is more prevalent in deep-living and planktonic

<sup>1</sup> R. E. Jentoft and R. Robinson, "The potassium-chlorinity ratio of ocean water," *J. Mar. Res.*, vol. 15, pp. 170-180, 1956.

<sup>2</sup> J. Boutin *et al.* *ESA Sea Surface Salinity Climate Change Initiative (Sea\_Surface\_Salinity\_cci): weekly and monthly sea surface salinity products, v2.31, for 2010 to 2019*, doi: doi:10.5285/4ce685bff631459fb2a30faa699f3fc5

<sup>3</sup> R. E. Jentoft and R. Robinson, "The potassium-chlorinity ratio of ocean water," *J. Mar. Res.*, vol. 15, pp. 170-180, 1956.

<sup>4</sup> J. A. Cotruvo, "Water desalination processes and associated health and environmental issues," *Water Cond Purif*, vol. 47, no. 1, pp. 13-7, 2005.

organisms than in benthic or shallow species. BL is caused by oxidation of a light-emitting molecule, called luciferin, in conjunction with a catalyzing enzyme such as luciferase or a photoprotein. BL organisms have widespread distribution in the sea from the surface to the deep sea, and from the poles to the tropics. BL emits in the blue-green wavelength range from 450-490 nm, with peak emission at about 470-480 nm. Light can shift to shorter wavelengths at deeper depths, and to longer wavelengths at shallow depths. These organisms can turn their photophores on and off, can modulate the intensity, color, and even the angular distribution of light. One study that collected data over 17 years reported that 76% of observed organisms in the water column have bioluminescent capability.<sup>1</sup>

Often organisms generate light in response to a mechanical stimulation, such as through the waves generated by a passing ship (shear forces) or the breaking of waves on the shore. The light is generally produced in short bursts from 50-500 ms duration at the peak wavelength of ~480 nm. Bacteria also emit light, but they do not respond to mechanical stimulation and thus are a constant, low-level source of background light. But for other organisms, a submerged instrument or vehicle that is not at neutral buoyancy and moving can generate light itself and so complicate measurements. An example of the wavelength range and distribution is shown<sup>2</sup> in Figure A.3.

The black lettered data is that which the authors' in the referenced paper measured, the data in red is compiled from the literature. The authors of Reference 1 also described the temporal behavior of mechanically stimulated BL. They noted a sharp rise in intensity with an exponential decay showing a half-life of ~1 second. There were some exceptions, noting that one example showed a longer half-life, one pulsed with a period of 0.5 second, and yet another turned on and off asynchronously. One constant in the literature is the statement of the difficulty of obtaining typical background BL spectra in situ since inserting instruments into the water often stimulates BL mechanically. Much of the data in the literature consists of sampling organisms at various depths and hauling these samples aboard research vessels where the BL is measured in an on-board laboratory.

The intensity of BL light varies with the sophistication of the organism. Luminescent bacteria emit  $10^3$  -  $10^4$  photons/sec. Dinoflagellates emit  $10^8$  -  $10^9$  photons/sec per 0.1 second flash, with a maximum intensity of  $10^{10}$  -  $10^{11}$  photons/sec. Larger organisms, such as jellyfish, octopus, or other fish, can luminesce at  $10^{11}$  photons/sec for seconds on end. Table A.2 provides some examples of the BL light in individual flashes and causes of BL emission for a small group of marine organisms.

---

<sup>1</sup> S. Martini and S. H.D. Haddock, "Quantification of bioluminescence from the surface to the deep sea demonstrates its predominance as an ecological trait," *Nature Scientific Reports*, **7**:45750 (2017); <http://dx.doi.org/10.1038/srep45750>

<sup>2</sup> S. Johnsen, T.M. Frank, S.H.D. Haddock, E.A. Widder, and C.G. Messing, "Light and vision in the deep-sea benthos: I. Bioluminescence at 500-1000 m depth in the Bahamian Islands," *J. Experimental Biology*, **215** 3335-3343 (2012); <http://dx.doi.org/10.1242/jeb.072009>

Table A.2. Total quantum emission of individual flashes by different marine bioluminescent organisms in response to a single stimulus (mean values).<sup>1</sup>

Group	Species	Mean total quantum emission (photons flash <sup>-1</sup> )	Intensity (W m <sup>-2</sup> at 1 m)	Wavelength (nm)	Duration (s)	Mode of stimulation	References
Copepoda	<i>Gaussia princeps</i>	$1.8 \times 10^{11}$				Electrical	Bowlby and Case (1991)
	<i>Pleuromamma xiphias</i>	$1.8 \times 10^{10}$				Mechanical	Latz et al. (1990)
	<i>Metridia lucens</i>	$1.7 \times 10^9$	$0.02 \times 10^{-9}$	480		Electrical	Clarke et al. (1962)
	<i>Metridia lucens</i>	$6.6 \times 10^{12}$	$32.4 \times 10^{-9}$	480		Mechanical	Clarke et al. (1962)
Euphausiacea	<i>Meganctyphanes norvegica</i>	$1.2 \times 10^{11}$	$0.3 \times 10^{-9}$	475		Electrical	Clarke et al. (1962)
	<i>Euphausia eximia</i>	$1 \times 10^{10}$				Vacuum	Lapota and Losee (1984)
	<i>Nyctiphanes simplex</i>	$1 \times 10^{11}$				Vacuum	Lapota and Losee (1984)
Amphipoda	<i>Cyphocaris faurei</i>	$5.7 \times 10^{10}$				Mechanical	Bowlby et al. (1991)
	<i>Scina crassicornis</i>	$3.1 \times 10^{10}$				Electrical	Bowlby et al. (1991)
Decapoda	<i>Acanthephyra purpurea</i>	$3.1 \times 10^{12}$	$25.2 \times 10^{-9}$	490	4	Electrical	Clarke et al. (1962)
Scyphozoa	<i>Periphylla periphylla</i>	$3.5 \times 10^{10}$	$0.49 \times 10^{-9}$	465	2.4	Electrical	Clarke et al. (1962)
	<i>Atolla wyvillei</i>	$1.2 \times 10^{11}$	$2 \times 10^{-9}$	470	2	Mechanical	Nicol (1958)
Siphonophora	<i>Vogtia glabra</i>	$1.4 \times 10^{11}$	$1.2 \times 10^{-9}$	470	4	Mechanical	Nicol (1958)
	<i>Vogtia spinosa</i>	$3.2 \times 10^{11}$	$1.68 \times 10^{-9}$	470	6.5	Mechanical	Nicol (1958)
Pyrosoma	<i>Pyrosoma atlanticum</i>	$2.3 \times 10^{13}$				Mechanical	Bowlby et al. (1990)

<sup>1</sup> S. Johnsen, T.M. Frank, S.H.D. Haddock, E.A. Widder, and C.G. Messing, "Light and vision in the deep-sea benthos: I. Bioluminescence at 500-1000 m depth in the Bahamian Islands," *J. Experimental Biology*, **215** 3335-3343 (2012); <http://dx.doi.org/10.1242/jeb.072009>

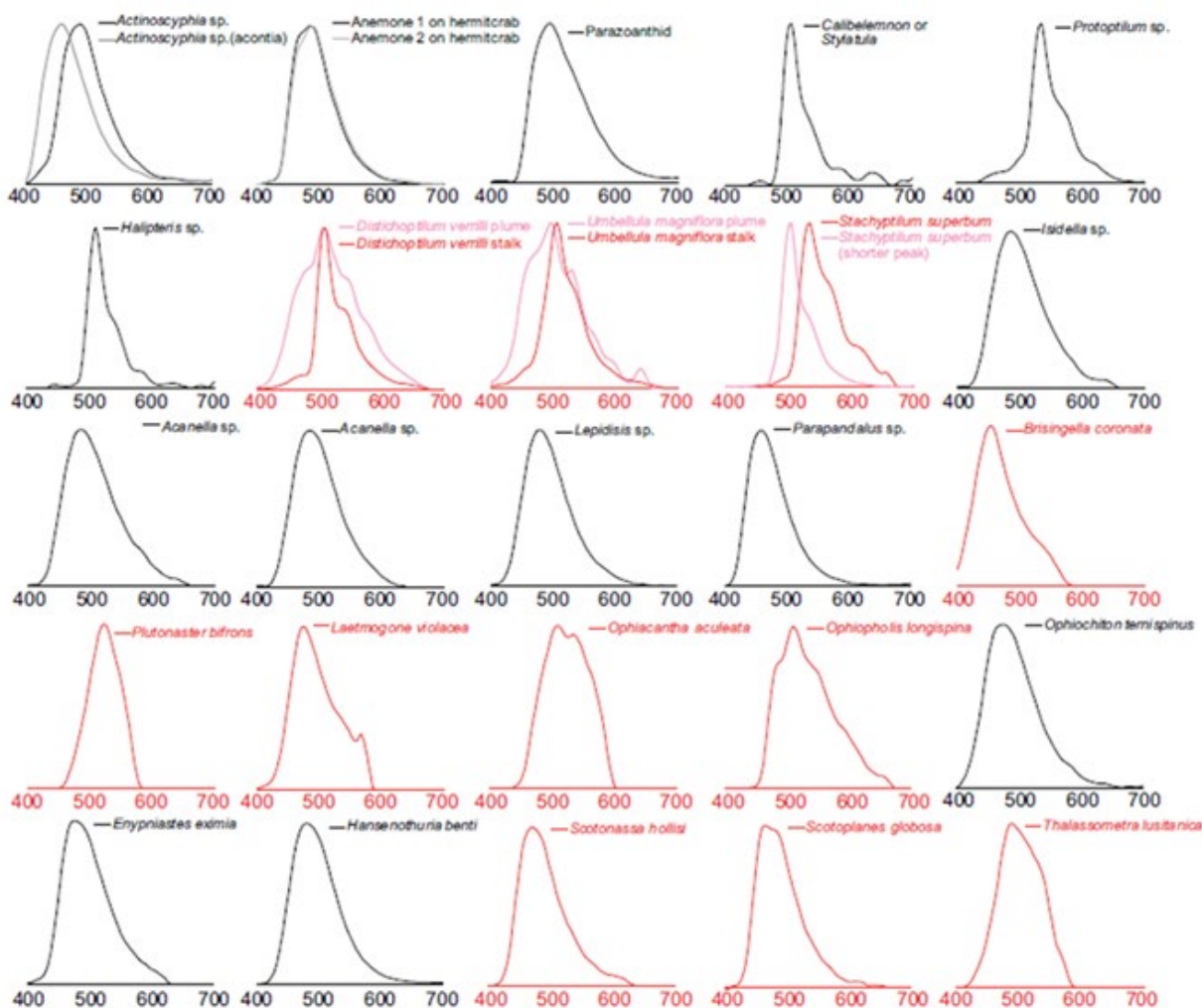


Figure A.3. Emission spectra of species collected by the authors in Reference 1 along with previously published spectra (in red).

The physics neutrino community has shown great interest in the origin and distribution of BL light as BL light emits with a wavelength range that overlaps with Cherenkov-generated light.<sup>1</sup> The authors of Reference 3 claim that BL light is rare, and is mostly caused by mechanical interactions with the optical modules of the ANTARES detection array, and/or the supporting structure of the array. BL varies by where you are in the world and at what depth you wish to operate. The authors also claim that it is not a large problem for ANTARES due to its 2.5 km depth and BL emissions can be distinguished from desired signals by signal processing of the array data. One significant observation is that BL light is seen on the downstream side of the optical modules with respect to the current or forward motion of the object (see Figure A.4 from Reference 2), which makes sense as BL organisms are stimulated to luminesce by shear

<sup>1</sup> I.G. Priede, A. Jamieson, A. Heger, J. Craig, and A.F. Zuur, "The potential influence of bioluminescence from marine animals on a deep-sea underwater telescope array in the Mediterranean Sea," *Deep Sea Research I*, **55** 1474-1483 (2008); <http://dx.doi.org/10.1016/j.dsr.2008.07.001>

forces from water flowing around the spherical module. To quote from Reference 2 with respect to the ANTARES optical module (OM):

*Most of the light output is likely to occur downstream of the OM owing to: time delay between stimulation and light output, development of highest stimulatory forces in vortices downstream of the OM, entrainment of organisms in the downstream vortices and mutual stimulation as these animals respond to one another.*

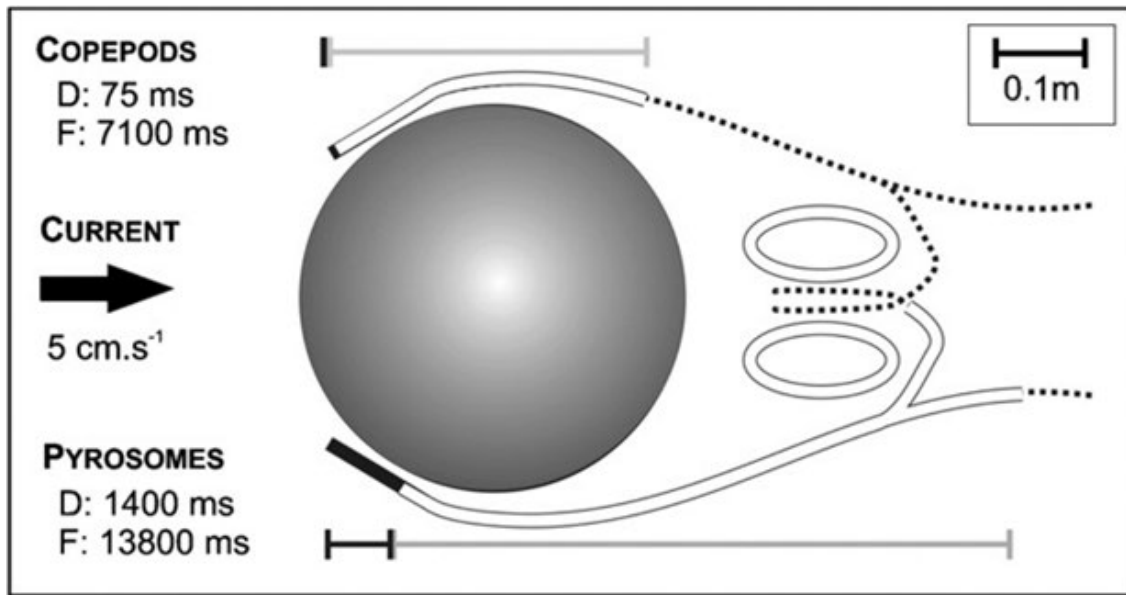


Figure A.4. Diagram showing the location of BL light with respect to an ANTARES optical module in a current of 5 cm/sec for two different organisms. D = delay of light, and F = flash duration

The Reference 2 authors present a model to predict the probability of bioluminescent organisms impingement on a sphere similar to the ANTARES optical modules. The expression they arrived at is shown below in Equation 1.

$$\frac{\text{Impacts}}{\text{sec}} = \pi \left( \frac{\phi_{\text{sphere}}}{2} + \frac{\phi_{\text{animal}}}{2} \right)^2 \times v \times \rho \tag{1}$$

Here, n is the current velocity in m/s, and r is the density of organisms per m<sup>3</sup>. The authors state that the BL emission will likely not occur due to impact because of the organisms’ sensory organs which will cause them to avoid the obstruction, but rather will respond to shear forces in the flow around the sphere to exceed a threshold described by Hartline *et al.*<sup>1</sup> The authors of Reference 2 also present an expression that predicts the natural occurrence of BL light flashes using the expression below in Eq. 2 which describes the interaction of BL and non-BL organisms such as plankton.

$$\frac{\text{Encounters}}{\text{sec}} = \frac{\pi R^2 \rho}{3} \cdot \frac{\mu^2 + 3v^2}{v} \tag{2}$$

<sup>1</sup> D.K.,Hartline, E.J. Buskey, P.H. Lenz, “Rapid jumps and bioluminescence elicited by controlled hydrodynamic stimuli in a mesopelagic copepod *Pleuromamma xiphius*”, *Biological Bulletin* **197**, 132–143 (1999); <http://dx.doi.org/10.2307/1542610>

Here,  $R$  is the encounter radius defined by the BL animal's sensory system,  $r$  is the density of other plankton,  $n$  is the swimming velocity of the BL animal and  $m$  is the swimming velocity of other plankton. The authors assumed that whenever a BL organism encountered a non-luminescent zooplankter, a luminescent event would occur.

## A.2 Effect of Thermoclines on Light Propagation

Thermoclines are regions in seawater marked by an abrupt change in water temperature. Our interest in the effects of thermoclines is since water temperature can affect the index of refraction of seawater as well as its salt content, which also affects index of refraction. These phenomena are important in underwater metrology involving the transmission of light as a change in index across a boundary can cause light to refract, be reflected due to the index contrast across the boundary, and perhaps even act as a light guide owing to total internal reflection when light traverses a denser medium with higher index to a less-dense medium having a lower index surrounding the denser region. These potential cases will be examined and evaluated for the challenges they might present in detecting Cherenkov light in seawater.

### A.2.1 Basic Theory

As discussed in the introduction, light can be affected in several ways due to a change in index across a boundary as may occur in a thermocline. The first is refraction, as governed by Snell's Law in Eq 1.

$$n_1 \sin \theta_1 = n_2 \sin \theta_2 \quad (1)$$

Snell's Law is also used to determine the angle of total internal reflection (TIR). For the case where  $n_1 > n_2$ , the angle of refraction at TIR is  $90^\circ$  and the sine of the angle is one. Therefore, the angle at which the onset of TIR occurs is given in Eq. 2.

$$\theta_{TIR} = \sin^{-1} \frac{n_2}{n_1} \quad (2)$$

For example, in water with  $n = 1.33$  bounded by air with  $n = 1$ , the TIR angle is  $\sin^{-1}(1/1.33)$  or  $48.75^\circ$ . Finally, light is reflected from surfaces where there is a change in index from the incident medium to the second medium. This behavior is described by the Fresnel equations. These equations describe reflection for two orthogonal polarization states of light in Eq. 3.

$$R_s = \left| \frac{n_1 \cos \theta_i - n_2 \sqrt{1 - \left(\frac{n_1}{n_2} \sin \theta_i\right)^2}}{n_1 \cos \theta_i + n_2 \sqrt{1 - \left(\frac{n_1}{n_2} \sin \theta_i\right)^2}} \right|^2 \quad (3)$$

$$R_p = \left| \frac{n_1 \sqrt{1 - \left(\frac{n_1}{n_2} \sin \theta_i\right)^2} - n_2 \cos \theta_i}{n_1 \sqrt{1 - \left(\frac{n_1}{n_2} \sin \theta_i\right)^2} + n_2 \cos \theta_i} \right|^2$$

In Eq. 3 the subscripts  $s$  and  $p$  refer to light polarized orthogonal to the plane of incidence (senkrecht) and light polarized in or parallel to the plane of incidence (parallel). At normal incidence, the Fresnel equations simplify to one equation shown below in Eq. 4.

$$R = \left| \frac{n_1 - n_2}{n_1 + n_2} \right|^2 \tag{4}$$

As an example, at normal incidence in air, the reflectance of water with  $n = 1.33$  is 2%. If we plot reflectance for both polarizations for water as a function of angle with air the incident medium, we obtain the results shown below in Figure A.5.

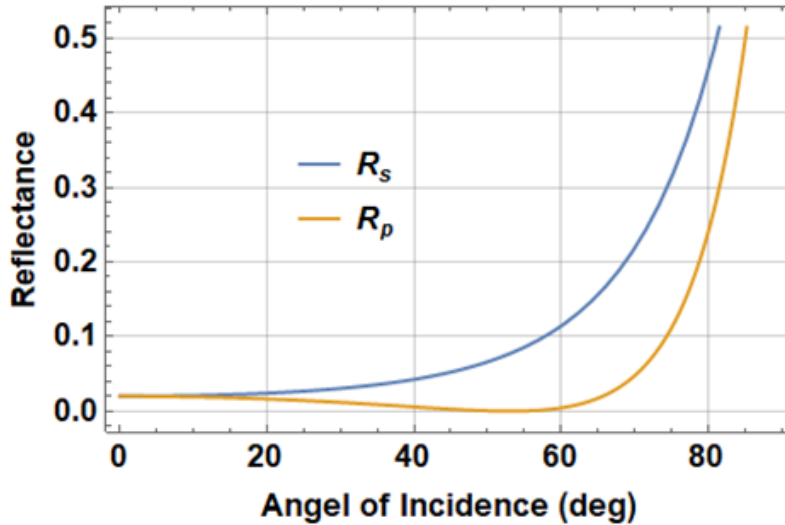


Figure A.5 Plot of reflectance versus angle of incidence for s- and p-polarized light for the case of water with  $n = 1.33$  with air the incident medium. Note that for p-polarization reflectance goes to zero at 53° angle of incidence. At this angle (Brewster’s angle), light is purely reflected at this angle of incidence for s-polarized light. This effect is exploited in gas laser windows to ensure light of one polarization with a high extinction ratio is emitted by the laser.

### A.2.2 Index of Refraction of Seawater and Effects on Light Propagation

Data for the index of refraction of seawater was obtained from a paper by the Scripps Institution of Oceanography (Table A.3). For our purposes, we consider the index at a wavelength of 480 nm (the peak of bioluminescent organism light as well as Cherenkov radiation), and extract one row from the paper at atmospheric pressure and salt content of 34.998%. Index decreases with a decrease in salt content, and it can be seen in the table below that index of refraction increases with a decrease in temperature.

Table A.3. Listing of the refractive index of seawater at a salinity of 34.998% and at atmospheric pressure.<sup>1</sup>

$\lambda$	Temperature °C						
480 nm	1.0	5.0	10.0	15.0	20.0	25.0	30.0
	1.34544	1.34525	1.34492	1.34450	1.34401	1.34345	1.34284

Suppose we consider a  $\Delta T$  of 20°C (resulting in a  $\Delta n$  of 0.0018) for a layer of 5.0°C seawater (1.34525) adjacent to a 25°C layer (1.34345). Using these two values of index of refraction the TIR angle is 87.04°.

<sup>1</sup> R. Austin and G. Halikas, “The Index of Refraction of Seawater,” Scripps Institution of Oceanography, January 1976.

Reflectance arising from light from a denser, colder layer incident on a warmer, less dense layer at normal incidence will result in a reflectance of 0.0000448%, which will not substantially reduce the amount of light that will reach a receiving instrument.

Now consider refraction from the denser medium to the less dense medium, invoking Snell's Law. For example, at 45° angle of incidence, the angle of refraction is 44.92° (light refracts away from the surface normal from a denser to less dense medium). The trend for all angles of incidence is shown below in Figure A.6. Note that refraction ceases at the TIR angle of 87.04°.

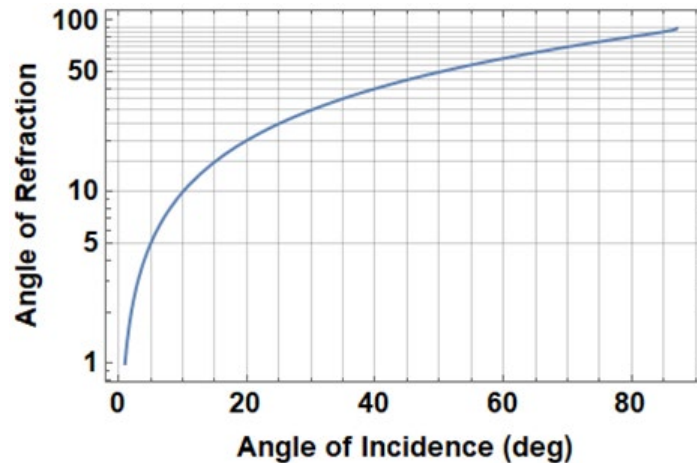


Figure A.6. Plot of angle of refraction from light originating in the colder, denser seawater with higher index of refraction into warmer, less dense seawater versus angle of incidence.

### A.2.3 Ray Deviation

Although the refraction from a typical thermocline has been shown to be almost negligible, it can, over the distance from the origin of the light to the target, deviate the light and cause the light ray to either miss the receiver or appear to come from a location other than its true location. If we consider the angular deviation in radians and multiply this by the range to the target, we obtain the ray deviation as a function of distance or range. For this we assume a spherical sensor with a 0.5 m diameter and find the distance at which the ray will just miss the sensor sphere. We can call this the walk-off distance. In practice the source is not a simple point source but an assemblage of point sources and so the receiver will still receive light but may ascribe the source location erroneously. This trend is displayed in Figure A.7. It can be seen that for even this small deviation arising from the small  $\Delta n$  of the example thermocline, at a distance 373 m range from the source and an angle of incidence of 45° to the thermocline boundary, the ray from a point source would completely miss a 0.5 m diameter sphere.

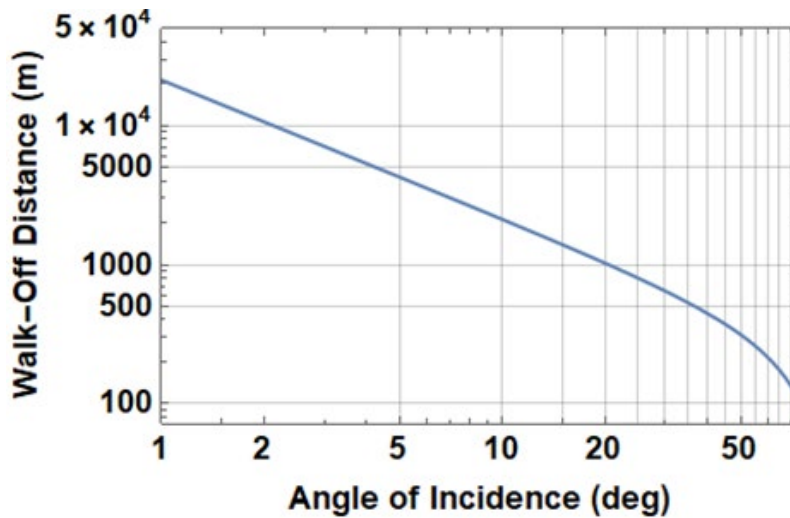


Figure A.7. Walk-off distance versus angle of incidence assuming a spherical receiver with a diameter of 0.5 m. At 45° AOI the walk-off distance is 373 m. At 75° AOI the walk-off distance reduces substantially to 99m.

#### A.2.4 Conclusions

Thermoclines result in a small index of refraction change between layers of water at different temperatures and/or salinity. Even for a  $\Delta T$  of 20°C the index change is very small ( $\Delta n = 0.0018$ ) and the chances of either reflective losses or reflection due to TIR affecting measurements substantially are small. These index changes will also refract light, albeit very little, but a ray (or wavefront) of light will deviate from the true direction from the source, and for large angles of incidence at a thermocline boundary, light can deviate enough to either miss the receiver aperture or more likely, appear to come from a direction other than its true direction. However, even this effect is small for likely scenarios and it must be concluded that the effect of a thermocline on received data will likely cause no serious complications in data acquisition and detection.

### A.3 Effectiveness of Polarization Filtering

It is well known that Cherenkov light is emitted into a cone with the trajectory of the particle moving along the axis of the cone. The light generated is linearly polarized in the plane of the cone's base, radiating outward and azimuthally symmetrical. At first blush it might seem that there would be no net polarization since all the outward radiating polarization vectors might cancel each other out but in practice, i.e., in a real measurement scenario, there will be a superposition of radiating cones, absorption and scattering by molecules in solution and dissolved solids, which will alter the polarization state and produce a net polarization. This may provide a method of excluding both bioluminescence background as well as  $^{40}\text{K}$ -induced Cherenkov light, which is isotropic and not expected to produce a net polarization. The final analysis as to whether polarization provides an advantage in detection will involve an analysis of signal-to-noise, as any polarization element will necessarily reduce the amount of light reaching the detector based on the polarization state of the light and the efficiency of the polarizer/analyzer. There are few papers in the literature concerning the polarization of Cherenkov light but the few that have been found so far will be summarized below.

#### A.3.1 Paper 1: A possible use for polarizers in Imaging Atmospheric Cherenkov Telescopes

The above paper by Calle *et al* was published in *Astroparticle Physics*, Volume 17, Issue 2, May 2002, Pages 133-149; [https://doi.org/10.1016/S0927-6505\(01\)00144-X](https://doi.org/10.1016/S0927-6505(01)00144-X) concerning Cherenkov light from Extensive Air Showers. A figure showing an air shower and production of Cherenkov light and a detail of a Cherenkov cone showing its polarization is below from Fig. 5 of the Calle paper.

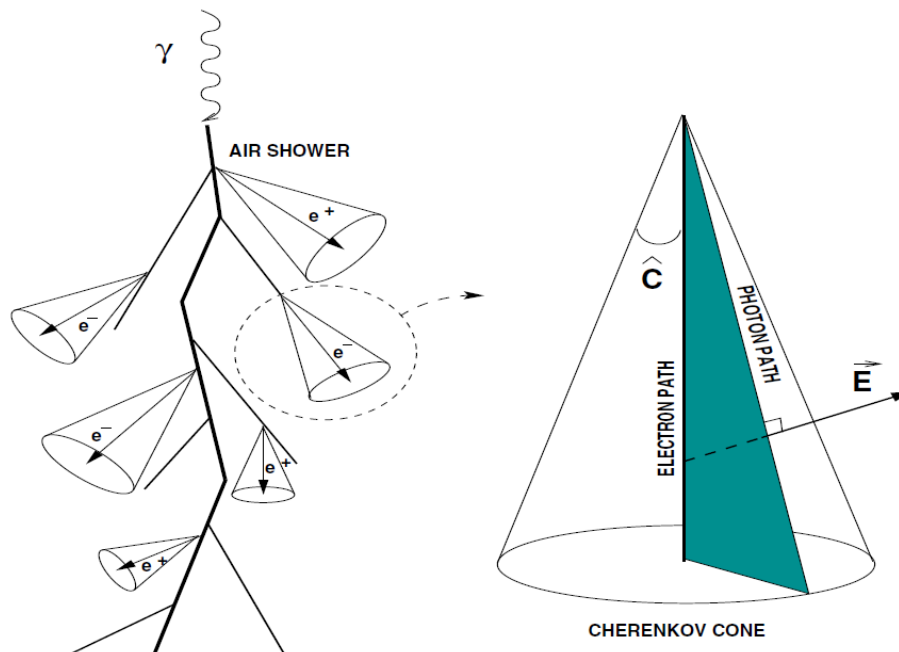


Figure A.8. Reproduction of part of Fig. 1 from the Calle paper cited above showing the production of single Cherenkov light cones (above left) and the orientation of the polarization vector relative to the Cherenkov cone.

The authors conclude that using polarizers on the camera helps exclude background light and can help increase the significance of very high energy  $\gamma$  signals by including polarizers on each PMT with their polarization axes pointing towards the center of the camera (telescope). The authors' relied on Monte Carlo simulations in Geant to reach their conclusions.

### A.3.2 Paper 2: Measurement of the Cherenkov light spectrum and of the polarization with the HEGRA-IACT-system

The above paper was by Döring *et al* Proceedings of ICRC 2001: 1. The paper includes experimental data acquired from the imaging atmospheric Cherenkov telescope (IACT). In it they show the polarization dependence as a function of  $r$ , the distance from shower core position to the central telescope. Two figures below summarize their results for  $r$  between 50 m and 70 m.

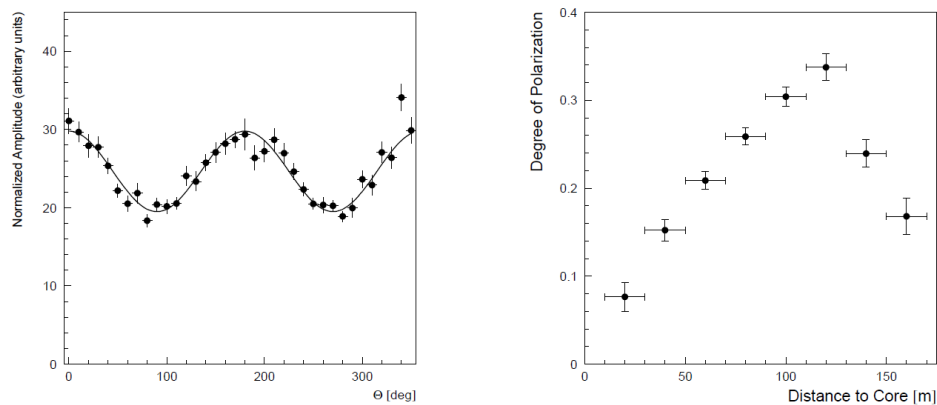


Figure A.9. Figures 4 and 5 from the cited paper. Normalized energy as a function of polarizer angle (above left) and Degree of Polarization (DOP) as a function of core distance. DOP is the normalized modulation  $(I_{\max} - I_{\min}) / (I_{\max} + I_{\min})$  of the polarization for a particular core distance.

The authors do not propose a use for these phenomena but promised a follow-up paper. I have not seen this paper yet after searching the literature.

### A.3.3 Paper 3: Accurate Dose Measurements Using Cherenkov Polarization Imaging

At the following link: <https://arxiv.org/abs/2106.08218> It does not appear to have been published. In this paper, the authors propose using polarization of Cherenkov light for accurate dose measurement in medical applications of radiation. The authors mention work that has been done using polarization to exclude fluorescence from the signal in carbon ion irradiation, and our application could use it to exclude biofluorescence if it were a problem. They performed an experiment using the following apparatus shown below.

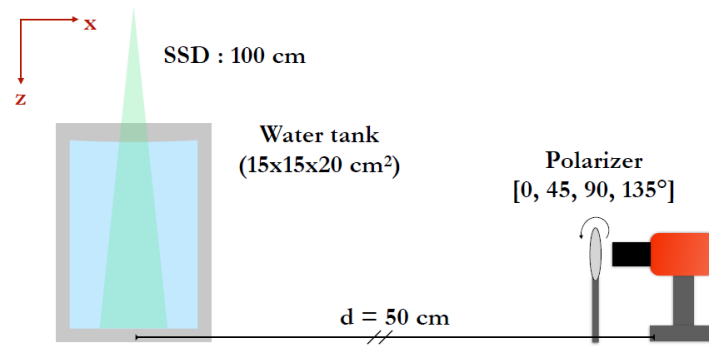


Figure A.10. Experimental setup for the paper listed above. The source was a 6 MV photon beam, 5 cm x 5 cm. The polarized acquired images with the polarization axes shown above.

The results of the experiment are shown below in Figure A.11, fit to the equation according to Malus' Law (intensity as a function of the angle of the polarizer and that of the angle of linear polarization).

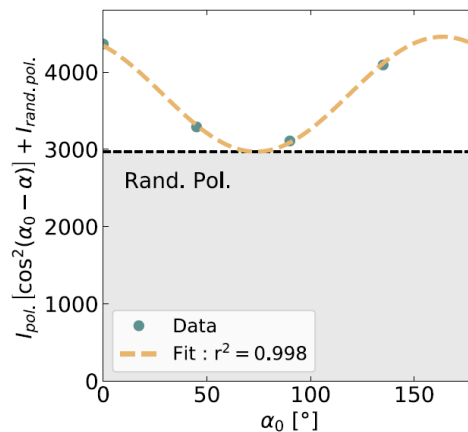


Figure A.11. Experimental data fit to the equation shown along the y-axis (Malus Law), which expresses the amount of Cherenkov light as a superposition of polarized and randomly polarized light.

Their hypothesis was that the dose was proportional to the polarized Cherenkov signal and further explanation in the paper bears this out. In this setup, they found that  $29 \pm 1\%$  of the signal was polarized.

In summary several papers have been found that investigate the polarization properties of Cherenkov light, both to suppress background, and in the case of the medical irradiation, to accurately estimate irradiation dose. The search will continue for other work in this area but perhaps the ability to suppress background may be the most useful application of polarization Cherenkov viewing in our application. What is surprising is that in none of these papers did the authors' use Stokes parameter formalism<sup>1</sup>, which is typically what one would do to put the results in a context that would be understandable by a wider audience.

<sup>1</sup> [https://en.wikipedia.org/wiki/Stokes\\_parameters](https://en.wikipedia.org/wiki/Stokes_parameters)

## A.4 Detector Design Options

Some Cherenkov detectors, for example, the optical modules (OM) used in the ANTARES neutrino experiment<sup>1</sup>, have no fore optics and simply mount a very large PMT (10" diameter) in a sphere. The name ANTARES comes from Astronomy with a Neutrino Telescope and Abyss environmental RESearch project. A photograph of an optical module is shown in Figure A.12.



Figure A.12. A photograph of the ANTARES optical module.

By mounting many of these OM in a 3D array and timing the arrival of Cherenkov light across the array, the muon direction may be determined. In our application there may only be a single optical module and so to determine direction of Cherenkov light multiple detectors in a spherical orientation could be used to determine the direction of received light, and also provide a reference background signal to determine the steady-state Cherenkov light produced by <sup>40</sup>K background as well as bioluminescent bacteria.

Each sensor will ideally have a CPC with a limited field of view (FOV) to segment the half space such that several will be combined to image a much larger FOV, but by analyzing the light detected in each module to determine the center of mass of the received light, the direction of the arriving light can be determined. An alternative approach that would only require one CPC might have a single aperture with a limited but large FOV with multiple detectors lining a sphere whereby the amount of light reaching each detector could help determine the direction of the arriving light.

Multiple zones could be explored by scanning the sensor mechanically. One drawback in this approach is that one no longer has access to a monitor channel to gauge ambient background from <sup>40</sup>K or bacterial bioluminescence. For either approach, the CPC allows one to collect at specified angles with the entrance aperture always larger than the exit aperture where one can mount the detector, either SIPM or PMT. This allows a smaller detector which reduces detector capacitance and reduces cost. Additionally, a square or rectangular CPC can be fabricated to better match the physical outline of SIPM elements, and

---

<sup>1</sup> P. Amram et al, "The ANTARES optical module," *Nuclear Instruments & Methods In Physics Research A*, **484**, 369-383 (2002); [https://dx.doi.org/10.1016/S0168-9002\(01\)02026-5](https://dx.doi.org/10.1016/S0168-9002(01)02026-5)

example of which is shown below that also only allows a FOV of  $\pm 30^\circ$ . As was shown in Figure A.13, a surface source was placed at the exit aperture and rays with a Lambertian distribution were emitted from the entrance aperture and the companion polar plot shows both the square profile as well as the  $\pm 30^\circ$  FOV.

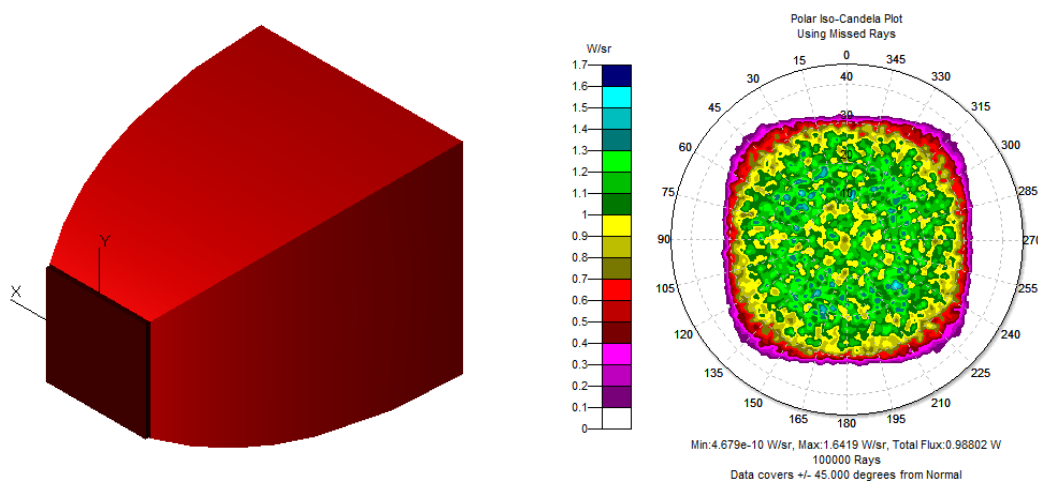


Figure A.13. A perspective view of a rectangular CPC is shown (above left) along with the emission profile when a Lambertian source is placed at the exit aperture and rays traced in the direction of the scene (above right).

#### A.4.1 Optical Design Considerations

Except for spent fuel rods in a cooling pond, the amount of Cherenkov light emitted through other means is expected to be small. Therefore, efficient concentration of the light onto the detector is paramount. It is known that the use of imaging optics to collect this light is not optimum and the preferred approach involves a branch of optics called nonimaging optics where the goal is to collect the maximum amount of light without regard to imaging quality or optical aberrations. One solution to this problem was discovered in 1966<sup>1</sup> with what was originally called a light funnel, but eventually was given the name *compound parabolic concentrator* or CPC. The CPC has a nearly maximum theoretical concentration ratio and is greatly superior to image-forming optics in this regard. Concentration ratio is defined in the equation below where  $a$  and  $a'$  are the radii of the entrance apertures, respectively, and  $\theta_i$  is the acceptance angle of the collector. The assumption is that every ray that enters the system that is equal to or less than  $\theta_i$  exits the collector. It can be seen for an acceptance angle of  $30^\circ$ , the concentration ratio can approach 2 for a CPC.

$$\frac{a}{a'} = \frac{1}{\sin \theta_i}$$

CPCs can be reflective or refractive or hybrid reflective/refractive, but reflective versions are easier to fabricate by creating a master using single point diamond turning and replicating copies via electroforming or molding, and they are also achromatic. The term parabolic in the CPC name refers to the walls of the device whose shapes are parabolic sections. The design equations typically used to determine the parameters for the CPC take the form shown below for the focal length of the device.

<sup>1</sup> H. Hinterberger and R. Winston, "Efficient Light Coupler for Threshold Cherenkov Counter," *Rev. Sci. Inst.*, **37** 1094 (1966); <https://doi.org/10.1063/1.1720428>

$$f = a'(1 + \sin \theta_{max})$$

Where,  $f$  is the focal length of the parent parabola,  $a'$  is the exit port radius of the CPC and  $\theta_{max}$  is the field of view (FOV) or input angle of the CPC. To determine the length  $L$  of the CPC, the expression shown in the equation below. One caveat to observe is that the smaller the input angle, the longer the CPC which may frustrate fabrication efforts by requiring an undesirably long boring bar for reflective designs.

$$L = \frac{a'(1 + \sin \theta_{max}) \cos \theta_{max}}{\sin^2 \theta_{max}} = \frac{f \cos \theta_{max}}{\sin^2 \theta_{max}}$$

Additionally, the equation of the shape of a CPC is given by the equation below where  $a'$  is the radius of the exit aperture,  $r = \sqrt{x^2 + y^2}$  and  $\theta_{max}$  is the acceptance angle which is the largest angle desired to exit the CPC (which can be as large as 90°).

$$(r \cos \theta_{max} + z \sin \theta_{max})^2 + 2a'(1 + \sin \theta_{max})^2 \cdot r - 2a' \cdot \cos \theta_{max} (2 + \sin \theta_{max})z - a'^2 (1 + \sin \theta_{max})(3 + \sin \theta_{max}) = 0$$

Design and modeling of the CPC's performance is accomplished most efficiently using a solid optics modeler such as TracePro<sup>1</sup>. For example, suppose we wish to mate the CPC to a 12.7 diameter PMT and desire a 30° maximum field of view angle. Using the expressions above we find the focal length,  $f$  to be 9.525 mm. To determine the length of the CPC using Eq. (3), we find  $L$  is 32.9956 mm. The resulting design and exit profile when rays are launched using a Lambertian surface source at the rear surface of the CPC is shown below in Figure A.14 confirming the CPC as a 30° FOV (half angle).

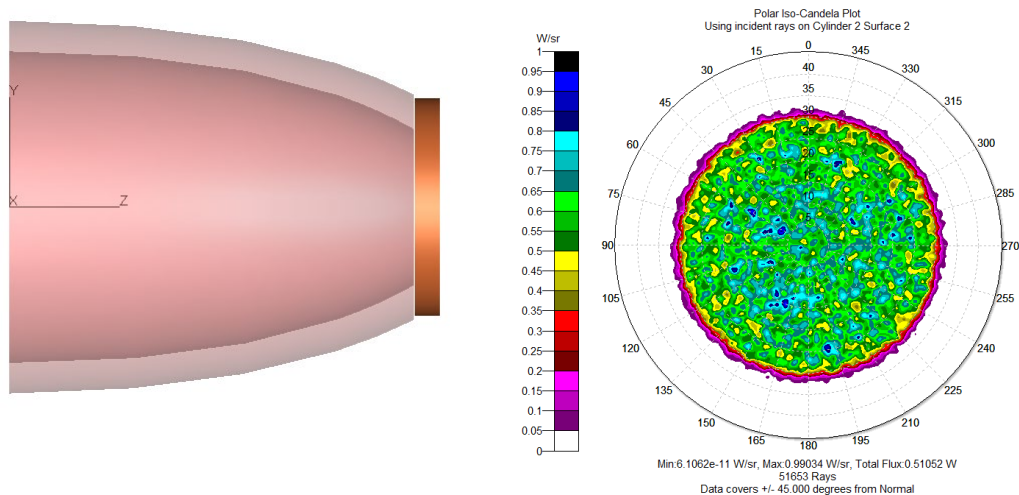


Figure A.14. Graphic showing the final design of the CPC (above right) and the ray pattern exiting the CPC if a Lambertian source is place at the exit aperture of the CPC and allowed to emit from the entrance aperture (above right).

<sup>1</sup> <http://www.lambdares.com/tracepro>

### A.4.2 Notional Detector Design

Below is an example of a sphere coupled to a CPC designed to admit rays diverging with an included angle of  $60^\circ$  ( $\pm 30^\circ$ ). In Figure A.15 the source is collinear with the optical axis of the sensor and emits uniformly with a half angle of  $30^\circ$  and we can see that if, for example, there were 4 detectors mounted at the extreme cardinal points of the sphere (north, south, east, and west) all would experience similar amounts of light detected. Note that in these figures the rays emitted from the point source are sorted to only show those that strike the interior of the sphere for clarity.

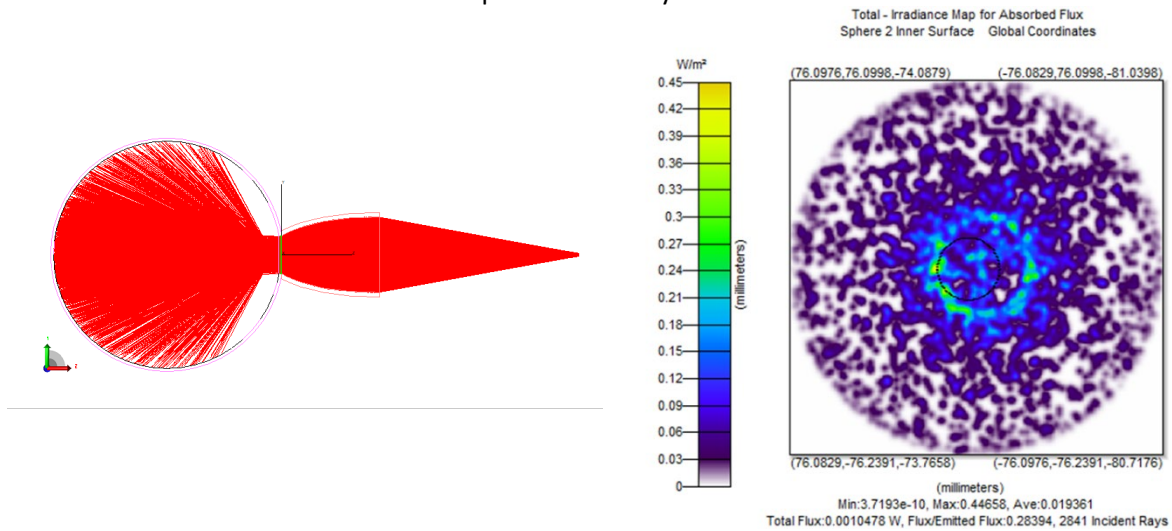


Figure A.15. CPC admitting rays within the  $60^\circ$  cone (above left) and striking the sphere interior (above right) for the source with emitting direction angle about X and Y axes of  $(0^\circ, 0^\circ)$ . All detectors (positioned at the points of the compass: north, south, east, and west) are illuminated equally.

For the next examples, the incident light will illuminate the sensor with angles (with respect to the X and Y axes of the coordinate system) at angles  $(+20^\circ, +10^\circ)$ ,  $(+20^\circ, -10^\circ)$ ,  $(-20^\circ, -10^\circ)$ , and  $(-20^\circ, +10^\circ)$ .

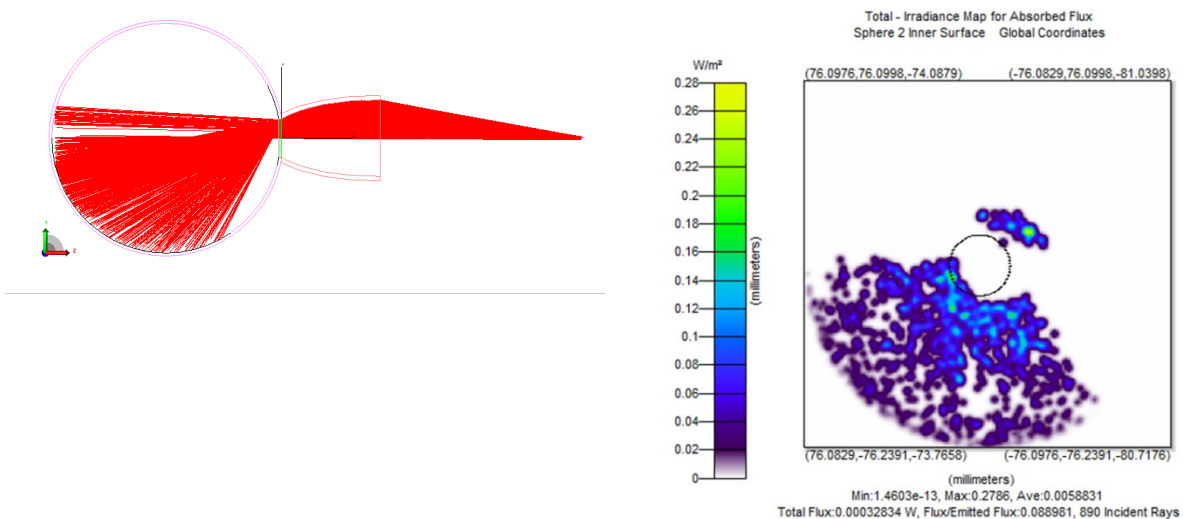


Figure A.16. Light emitted with angles  $(+20^\circ, +10^\circ)$  (above left) and its pattern on the sphere wall (above right).

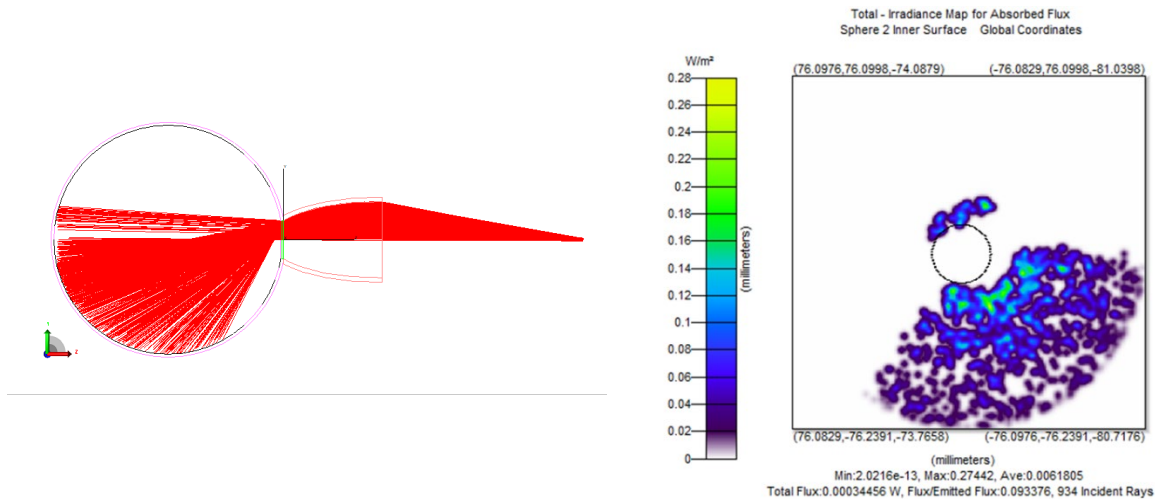


Figure A.17. Light emitted with angles (+20°, -10°) (above left) and its pattern on the sphere wall (above right).

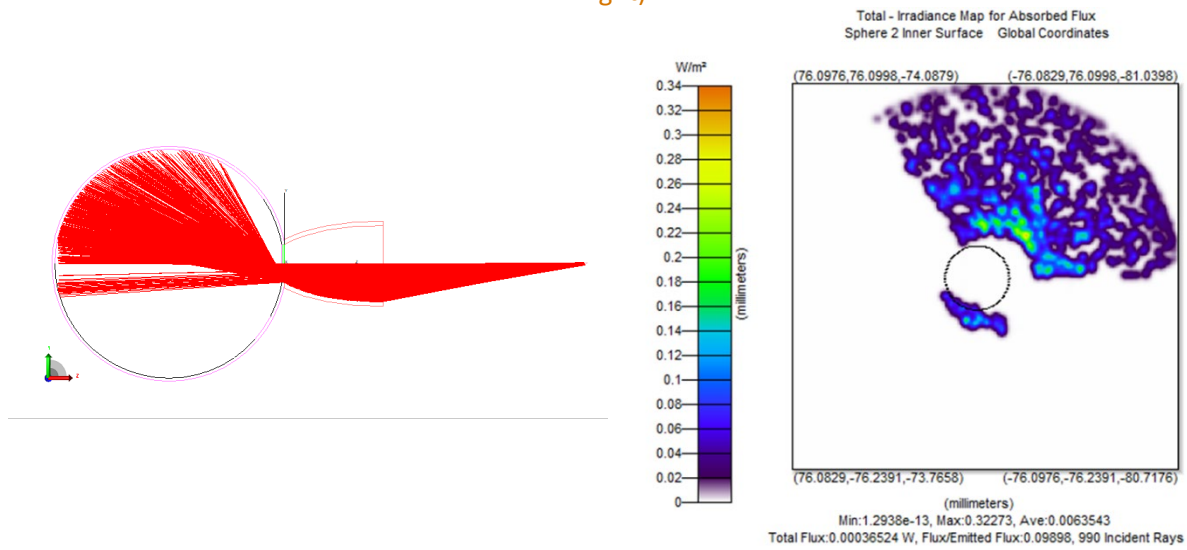


Figure A.18. Light emitted with angles (-20°, -10°) (above left) and its pattern on the sphere wall (above right).

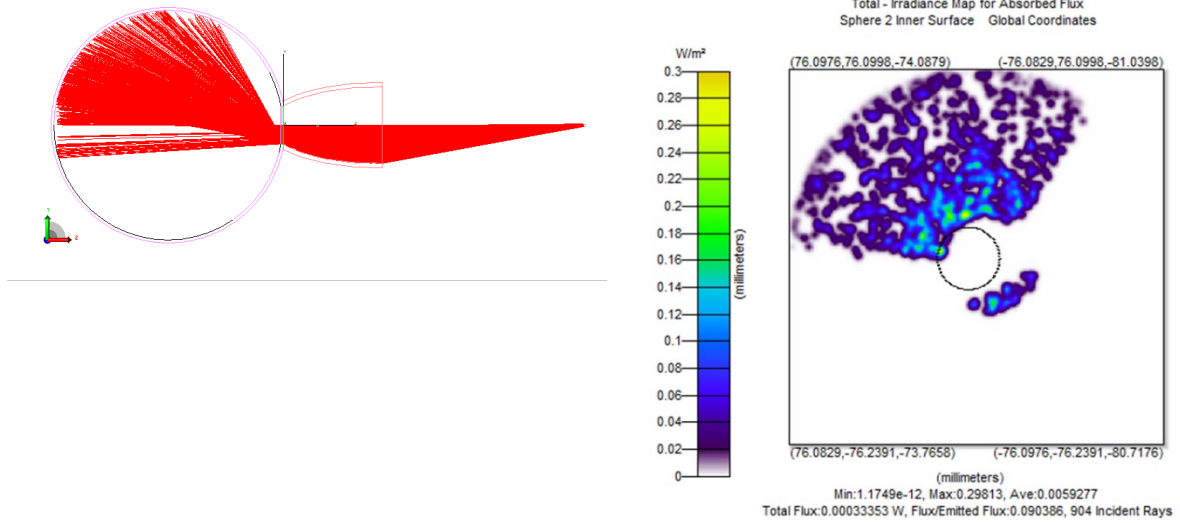


Figure A.19. Light emitted with angles (-20°, +10°) (above left) and its pattern on the sphere wall (above right)

With the notional design example, one approach to determining the source location and heading can be achieved using a single CPC and multiple detectors, but the same result could also be accomplished with a spherical design having individual CPCs for each detector.

# **PacificNorthwest National Laboratory**

902 Battelle Boulevard  
P.O. Box 999  
Richland, WA 99354  
1-888-375-PNNL (7665)

***[www.pnnl.gov](http://www.pnnl.gov)***